Article:
Zajac, M, Skocek, J, Adu-Amankwah, S et al. (2 more authors) (2018) Impact of microstructure on the performance of composite cements: Why higher total porosity can result in higher strength. Cement and Concrete Composites, 90. pp. 178-192. ISSN 0958-9465

https://doi.org/10.1016/j.cemconcomp.2018.03.023

Impact of microstructure on the performance of composite cements: why higher total porosity can result in higher strength

Maciej Zajac[1], Jan Skocek[1], Samuel Adu-Amankwah[2], Leon Black[2], Mohsen Ben Haha[1]

[1] HeidelbergCement Technology Center, Oberklamweg 2-4, 69181 Leimen, Germany
[2] Institute for Resilient Infrastructure, School of Civil Engineering, University of Leeds, Woodhouse Lane, Leeds, LS2 9JT, UK

Abstract
This paper describes the underlying principles behind the evolution in performance of ternary composite cements comprising Portland cement clinker, slag and limestone. By using the predicted phase assemblage as an input for the micromechanical model, the mechanisms underlying the evolution of mortar strength and Young's modulus were analyzed and quantified. This allowed the roles of hydrate assemblages and porosity distribution on the evolution of performance to be explained and quantified. Slag hydration results in the formation of a microstructure more efficient for development of compressive strength and elastic stiffness. Limestone further improves microstructure and enhances reactivity of the systems studied.

Keywords
Modelling; Continuum micromechanics; Hydration; Porosity; Slag; Limestone

1. Introduction

Composite cements are the most commonly used cement types in the building industry. The first generation of composite cements, i.e. two components (binary) systems, are now being replaced by ternary and quaternary systems, in which the clinker content has continuously decreased while the number of supplementary cementitious materials has increased [1] [2]. The hydration of the Portland cement clinker occurs simultaneously with the reactions of the supplementary cementitious materials (SCMs) [3], mutually influencing the reactivity of the components and impacting on the resulting hydrate assemblage and microstructure [3]. Research on hydration kinetics has revealed that SCMs impact the reaction kinetics and extent of the clinker reactions [4]. Later studies showed that simultaneous hydration of different SCMs in ternary and quaternary blends is complex since SCMs influence the hydration of other SCMs [5]. This requires a better understanding of the hydration processes and interdependencies in order to better predict performance of multi component composite cements [6][7]. The ability to predictively model the performance of these new cements is of utmost importance since the prescriptive approaches of the concrete industry, based mainly on experience gained with Portland cement concrete, will not be applicable to the new cements. Presently, modelling approaches are used to improve understanding of the hydration process and to correlate the predicted hydrates assemblages with cement performance [8].

Hydration models are well established, particularly based on the thermodynamic approach [9]. The use of thermodynamic calculations allows investigation of the effect of different variables e.g. changing composition of composite cements [10] [11] [12] [13] [14] [15] [16] or of temperature [17] [13] on the phase assemblage of cement systems. Using the kinetics of anhydrous phase dissolution enables calculation of the evolution of phase assemblage over time [18] [19] [20] [21]. Additionally, when incorporating the density of the anhydrous phases and hydrates, thermodynamic modelling also allows the volumes of solids, solution and chemical shrinkage to be determined [9]. Hence, thermodynamic modelling allows the impact of various parameters [9] on the pore volume evolution to be studied.

Performance models are not so well established. Most often, a semi-empirical relationship between total porosity, or a comparable simple measure, and strength is used for a given cement type or group of comparable cements (e.g. [22] [13] among others). Such models, however, generally struggle to predict the performance outside of the range used for their calibration. Recently, modelling approaches based on continuum micromechanics have been developed for upscaling of strength of cementitious materials [23][24]. Such models are capable of reflecting changes to hydrate assemblages and microstructure caused by the use of SCMs. With their relatively low complexity, low computational costs and general applicability, the micromechanical models have quickly established their role in industrial applications of cementitious materials, ranging from tunnel construction to cement optimization [25][24][26][23][27][28][29].

In our earlier paper [30], we have reported how the cement components have a pronounced impact on the hydration of each other and on the resulting microstructure. In this paper, we have applied a modeling framework to explain and predict the performance evolution of ternary composite cements comprising Portland cement clinker, slag and limestone. The framework consists of the thermodynamic model for cement hydration and the micromechanical model for strength upscaling [31]. This has allowed us to correlate the porosity evolution measured by different techniques with the evolution of mechanical performance and has further provided basis for identification and quantification of the underlying mechanisms.

2. Materials

Composite cements (binders) were prepared from a commercial CEM I 52.5 R, ground granulated blast furnace slag and natural limestone. Additionally, natural anhydrite was used to fix the overall SO_3 level of the composite cement to 3 %. Additionally, in some instances, natural quartz sand was applied as an inert reference material for the SCMs. The chemical composition of the materials is given in Table 1.

Table 1 Chemical composition of the investigated samples

Composition	CEM I	Slag	Limestone	Quartz	Anhydrite
SiO_2	20.4	34.9	2.0	99.8	2.0
Al_2O_3	5.6	11.6	0.8	0.0	0.6
TiO_2	0.3	1.1	0.0	0.0	0.0
MnO	0.1	0.3	0.0	0.0	0.0
Fe_2O_3	2.5	0.5	0.3	0.0	0.2
CaO	62.1	41.8	53.1	0.0	38.3
MgO	1.7	5.8	0.6	0.0	1.5
K_2O	0.7	0.5	0.1	0.0	0.2
Na_2O	0.1	0.1	0.0	0.0	0.0
SO_3	3.5	3.1	0.1	0.0	52.2
P_2O_5	0.1	0.0	0.0	0.0	0.0
LOI	2.0	(+0.8)*	42.3	0.2	3.7
Sum	20.4	99.7	99.5	100.0	98.8

*-oxidation of sulfide

The mineralogical composition of the materials determined by Rietveld analysis is shown in Table **2** and Table 3, respectively.

Table 2 Clinker content of CEM I 52.5 R (wt.-%)

Phase	C_3S	C_2S	C_3A	C_4AF	Calcite	Anhydrite	Bassanite	Others

CEM I	58.1	14.3	9.2	6.7	1.9	1.7	3.0	5.1

Table 3 Mineralogical composition of supplementary materials (wt.-%)

Phase	Calcite	Quartz	Dolomite	Anhydrite	Amorphous/Others
Slag	2.4	0.1	-	-	97.5
Limestone	96.6	0.4	1	-	2.0
Quartz	0.5	99.5	-	-	-
Anhydrite	-	2.1	5.5	91.0	1.4

The particle size distribution of all the constituent materials, as measured by laser granulometry, is shown in Figure 1. The quartz and slag (of two finenesses: normal: S and fine: Sf) were ground in a laboratory ball mill. Other materials were received already ground.
The composite cements were prepared according to Table 4 by blending the constituent materials in a roller ball mill with plastic grinding media to improve the homogenization.

Table 4 Composition of binders investigated (wt.-%)

Binder designation	CEM I 52.5 R (C)	Slag/Quartz (S/Sf/Q)	Limestone (L)	Anhydrite
C	100	-	-	-
C-S	50.68	47.08 (S)	-	2.24
C-Q	51.84	48.16 (Q)	-	-
C-S-L	51.18	38.03 (S)	8.55	2.24
C-S-2L	51.18	28.53 (S)	18.06	2.24
C-Sf-2L	51.18	28.53 (Sf)	18.06	2.24

Note: The commercial CEM I 52.5 R cement contained 1.9% calcite and 4.8% calcium sulphate, which were accounted for when maintaining the 50:50 clinker:SCM ratio.

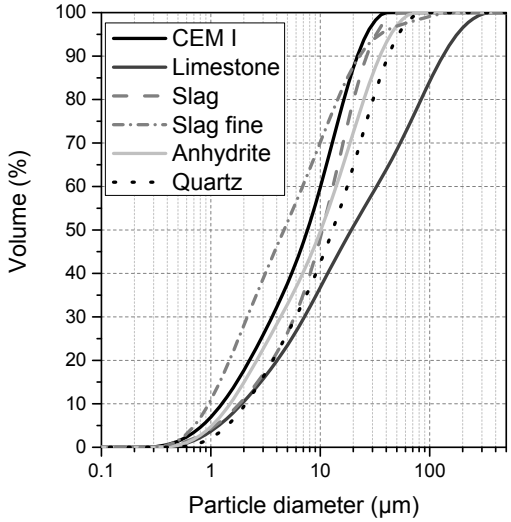

Figure 1 Particle size distribution of constituent materials

3. Methods

3.1. Experimental techniques

A multi-technique approach was used to follow the hydration of the binders. This included calorimetry, thermogravimetric, mercury intrusion porosimetry (MIP), scanning electron microscopy (SEM) and XRD supplemented with Rietveld and PONKCS methods. These techniques give quantitative as well as qualitative information about the hydration kinetics and phases formed. Details are given elsewhere [30].

Mortar samples with w/b of 0.5 were used for assessment of strength development, as prescribed in EN-196. The samples were cured under water. An additional set of samples was cured at 95 % RH to follow the development of Young's modulus using a Proceq Pundit PL-200PE device equipped with 250 kHz shear wave transducers. After 180 days of curing, three mortar prisms were tested according to the water porosity method [32]. This enabled determination of sample volume and density, the volume of compaction voids, plus the amount of water accessible porosity and empty porosity at 95 % RH.

3.2. Thermodynamic modelling

Thermodynamic modeling was used to calculate the evolution of hydrate assemblages, from which hydrate volumes could be determined. Thermodynamic modelling was carried out using the geochemical modelling program GEMS [33] [34] with thermodynamic data from the PSI-GEMS database [35] [36] supplemented by cement specific data [37] [38] [39].

The model was applied as described elsewhere [18] [19]. The dissolution kinetics of anhydrous phases was mathematically described with multi-parametric smooth functions. The input was based on experimentally determined dissolution kinetics of clinker phases and slag, as reported elsewhere [30]. Quartz was assumed to be inert. Hence, the composition of the hydrate assemblage was predicted based on the degree of reaction of the cement clinker and the slag as a function of time, assuming thermodynamic equilibrium at each stage of hydration. The following assumptions were introduced into the model:

- All anhydrous phases were assumed to dissolve congruently
- Calcite and gypsum contents were calculated to dissolve freely, i.e. without prescribing their dissolution degrees. Their amounts at equilibrium resulted from the availability of reacted alumina.
- C-S-H composition was corrected with Al incorporation to account for Al-uptake determined experimentally [30], without altering its thermodynamic properties.

It should be noted that the volume of the C-S-H phase does not include the gel porosity associated with this phase, but only the interlayer water [39], it will be further referred to as the solid C-S-H.

3.3. Mechanical modelling

A continuum micromechanics model, based on the work of Termkhajornkit [24], was applied. The micromechanical model takes the volumes of hydrates and porosity as predicted by the thermodynamic model, together with assumptions about spatial arrangement of hydrates, as an input. It can therefore reflect, in a physically well-substantiated manner, multiple parameters simultaneously. The material parameters, homogenization levels and other particularities were as used previously [31]. The key features of the model are as follows:

- The solid C-S-H volume, predicted by the thermodynamic model, is homogenized together with the porosity fraction which is saturated at 95 % RH as the first homogenization level.
- The next homogenization level consists of the remaining fraction of porosity, all other hydrates as well as anhydrous cement components embedded in the homogenized matrix from the first level.

- The last homogenization level comprises the homogenized matrix from the second level with sand and compaction voids added.

Note that the porosity partitioning based on its saturation at 95 % RH is the key difference to other similar models. Since the porosity saturation was measured only after 180 days, we assumed that the ratio between the saturated and empty porosity remained constant. All other particulars of the model were kept as elsewhere [31].

4. Results

4.1. Hydration – selected experimental results

The key experimental results characterizing the hydration process of the systems studied are presented below. A complete set of experimental data can be found elsewhere [30].

The hydration kinetics of the cement clinker is shown in Figure 2. In the plain Portland cement, the hydration degree of the cement clinker reached ~60 % at 1 day and ~90 % at 180 days. In the composite cements, early clinker hydration was accelerated, particularly in the presence of limestone. However, by 180 days, the final hydration degree was comparable for all investigated binders.

The slag reacted more slowly than the cement clinker (Figure 3). After one day, its hydration degree was about 30 % and increased up to ~60 % at 180 days. The presence of limestone and fine grinding of the slag resulted in an acceleration of the slag reaction. The overall hydration degree of the composite cements was always lower than the plain Portland cement paste (sample C).

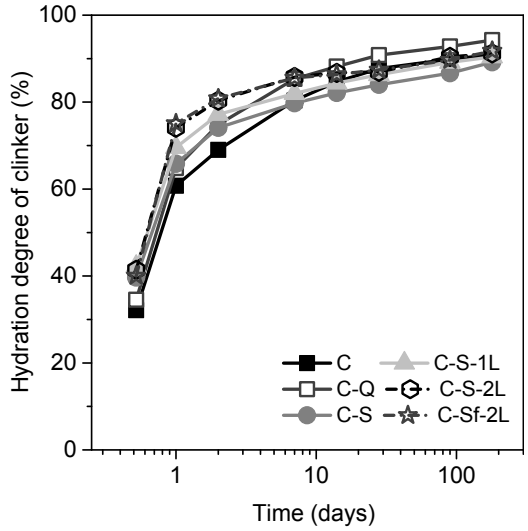

Figure 2 Evolution of the hydration degree of cement clinker by QXRD. The representative error is assumed to be ±2 % of hydration degree [30].

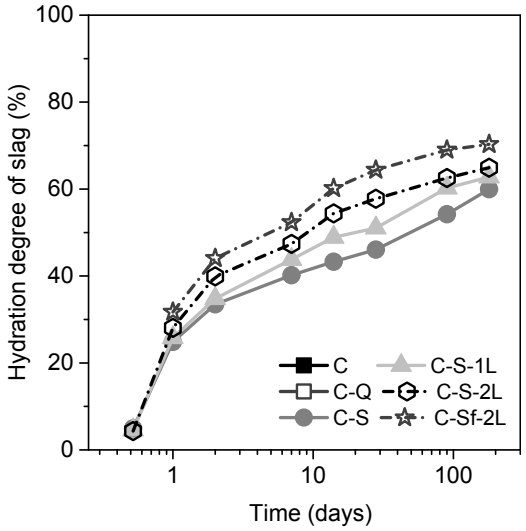

Figure 3 Evolution of the hydration degree of slag. The representative error is assumed to be ±5 % of hydration degree [30].

The bound water content is shown in Figure 4. For all samples, bound water content increased with time, but was always highest for the reference plain Portland cement and lowest for the quartz containing sample. For all the composite cements, the bound water contents were similar, being between that of the plain Portland cement and C-Q sample. The lower bound water content of slag containing binders may be associated with the lower overall hydration degree of these binders. However, due to the differences in chemical composition of the binders studied and hence of the hydrates formed, the bound water content could not be quantitatively linked to the hydration degree [40].

Figure 5 shows the low-angle XRD patterns after hydration for 180 days. The hydrates formed were typical for the systems investigated. The aluminate phases resulted in the precipitation of ettringite, plus hemi- and mono-carbonate phases. Since all the binders contained some calcite, there was no significant precipitation of monosulfate. However, increasing levels of additional limestone resulted in the formation of mono-carbonate over hemi-carbonate. Additionally, ettringite contents were similar for all binders since their SO_3 levels were set to be constant, the exception was sample C-Q, which was characterized by a lower SO_3 content. The reaction of silicate phases resulted in the formation of C-S-H, and portlandite, as reported earlier [30].

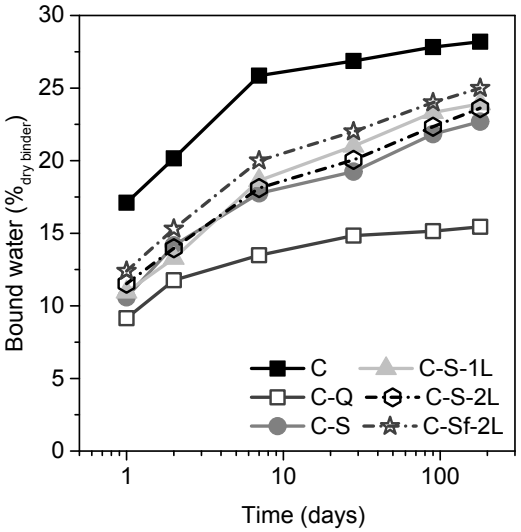

Figure 4 Evolution of the Bound water in the investigated samples. The representative error is estimated to ±1 %.

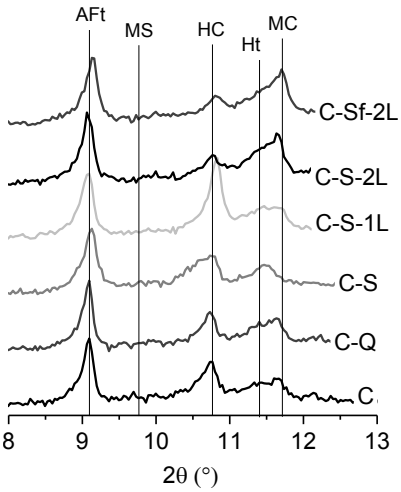

Figure 5 XRD-patterns for the different tested blends at 180 days. The main peaks of ettringite (AFt), monosulphate (MS), hemicarbonate (HC), monocarbonate (MC) and hydrotalcite (Ht) are indicated

4.2. Thermodynamic modelling of phase assemblage evolution

The predicted hydrates included C–S–H, CH, AFt and AFm phases, plus a small amount of hydrotalcite-like phase and iron-bearing hydrogarnets, as shown in Figure 6. In the plain Portland cement sample, the model predicted formation of hemi-carbonate and mono-sulfate because of the small quantity of calcite present. When comparing samples C and C-Q, the lower hydrates volume is clearly visible in the latter. However, the phase assemblage is qualitatively identical. The presence of slag in place of quartz results in a significant increase in C-S-H content. Compared to the plain Portland cement paste, the slag containing sample has lower contents of C-S-H, portlandite as well as AFm phases. The lower AFm content arises due to the consumption of Al to form C-S-H and hydrotalcite phase. Addition of limestone induces the stabilization of mono-carbonate.

Confirming the XRD data shown in Figure 5, modelling shows the presence of ettringite in all the investigated binders. Beyond 1 day of hydration, the content of ettringite does not change significantly. This is because of the aforementioned presence of small quantities of limestone in the CEM I used and further additions of limestone into the composite cements. The modelled ettringite contents in all samples, with the exception of C-Q, are similar because of the similarity in the total SO_3 levels. Additionally, in the case of slag-containing binders, the high incorporation of alumina into C-S-H reduces the amount of AFm phases formed which also contributes to the ettringite stabilization.

The modelling results agree well, both qualitatively and quantitatively (comparison not shown), with the experimental results discussed above, and reported previously [30].

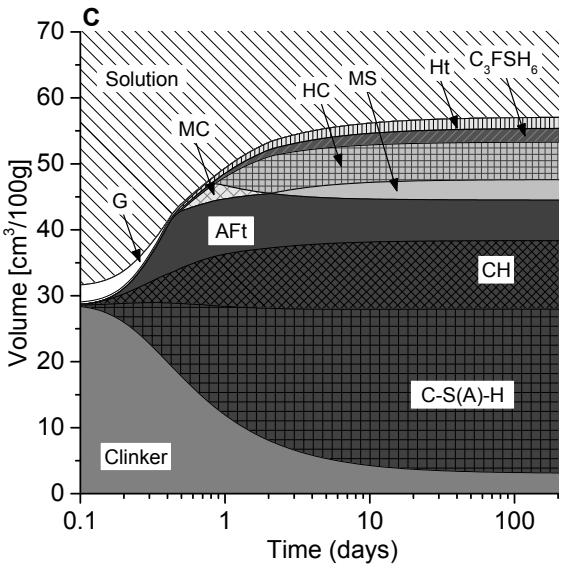
C
Solution
MC
HC
MS
Ht
C3FSH6
G
AFt
CH
C-S(A)-H
Clinker
Volume [cm3/100g]
Time (days)

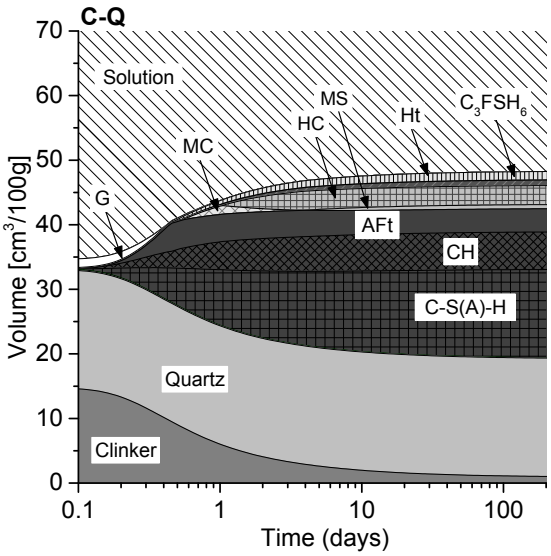
C-Q
Solution
MC
HC
MS
Ht
C3FSH6
G
AFt
CH
C-S(A)-H
Quartz
Clinker
Volume [cm3/100g]
Time (days)

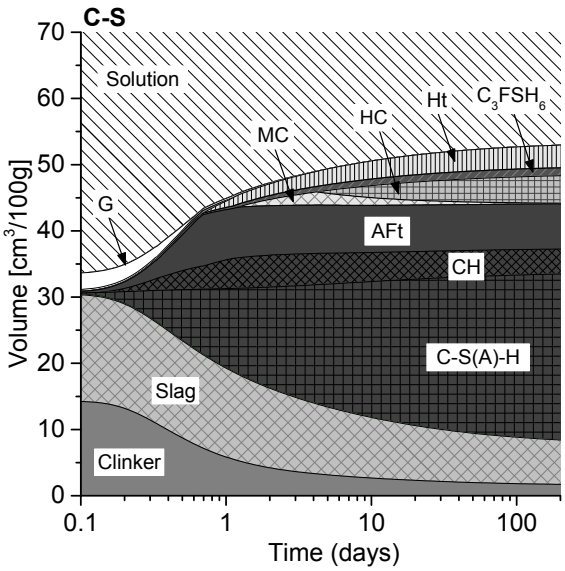
C-S
Solution
MC
HC
Ht
C3FSH6
G
AFt
CH
C-S(A)-H
Slag
Clinker
Volume [cm3/100g]
Time (days)

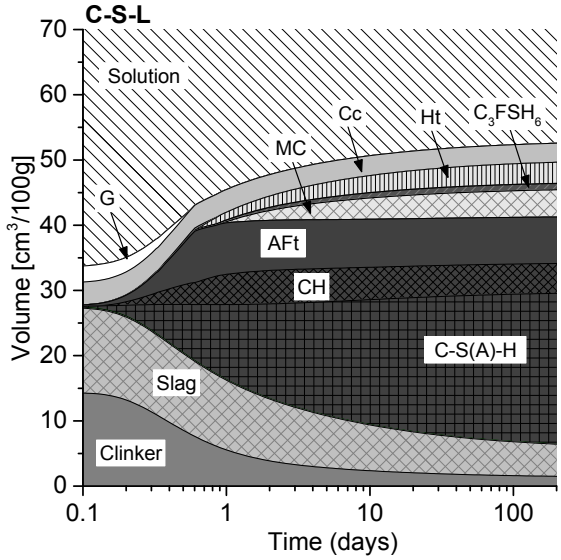
C-S-L
Solution
MC
Cc
Ht
C3FSH6
G
AFt
CH
C-S(A)-H
Slag
Clinker
Volume [cm3/100g]
Time (days)

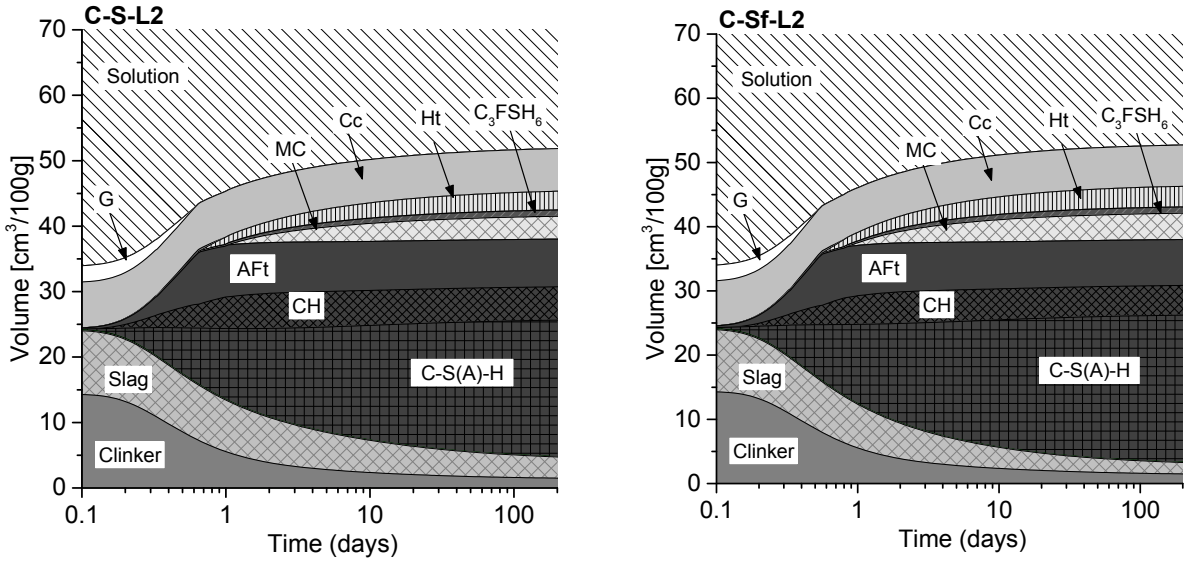

Figure 6 The volume of the different phases as function of time in hydrating binders modelled by GEMS. C-S(A)-H; C-S-H phase with modelled incorporation of alumina, CH – portlandite, AFt – ettringite, MC – Monocarbonate, HC – hemicarbonate, Cc – calcite, Ht – hydrotalcite, C_3FSH_6 – iron containing hydrogarnets, G – gypsum.

4.3. Compressive strength evolution

The compressive strength evolution of mortars is presented in Figure 7.

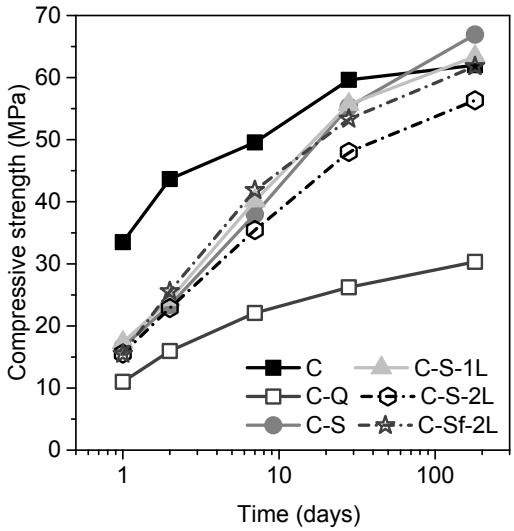

Figure 7 Evolution of the compressive strength

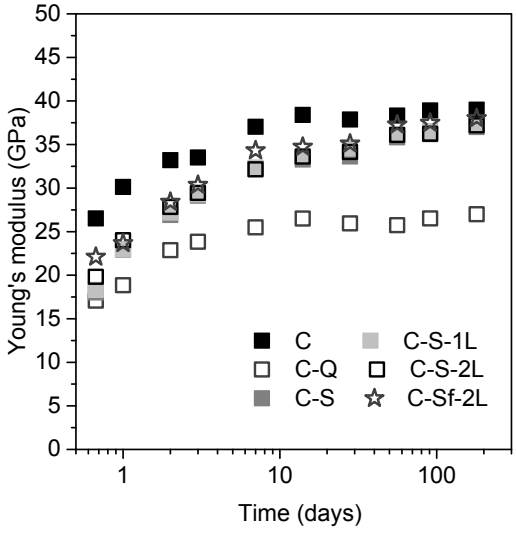

Figure 8 Evolution of the Young's modulus

The plain Portland cement achieved a compressive strength of 33 MPa after 1 day and 62 MPa after 180 days. The strengths of all of the composite cements were significantly lower at 1 day, at approximatively 15 MPa. However, their strength gain beyond this point was more rapid than for the plain Portland cement, such that they finally reached levels comparable to the sample C by 180 days. It is noticeable that the strength of samples C-S and C-S-1L were similar during the first 28 days, i.e. the replacement of 10 % slag by limestone had no negative impact on the strength development. A further reduction in the slag content with an increase in limestone content however brought a diminished strength gain from 7

days and beyond (sample C-S-2L). This effect could be offset by fine slag grinding, as seen for sample C-Sf-2L. The compressive strength of quartz containing samples was always lower than their slag/limestone analogues.
The evolution of Young's modulus is shown in Figure 8 and reveals similar trends as discussed for the compressive strength evolution. However, the increase in performance beyond two weeks of hydration was less pronounced.

4.4. Evolution of porosity

Figure 9 shows typical SEM-BSE micrographs of the samples after hydration for 180 days. All samples showed an intimate mixture of anhydrous material, different hydrated phases and pores. In the composite cements, quartz (C-Q), slag (C-S and C-S-2L) and limestone (C-S-2L) particles were visible. The slag particles were larger, with characteristic, partially hydrated rims. The more noticeable hydrates included calcium hydroxide appearing light grey, and outer product C-S-H, appearing dark grey. Samples C and C-S showed very dense microstructures, with little porosity. Sample C-Q was characterized by significantly darker regions, reflecting its greater porosity than the other samples. Sample C-S-2L showed an intermediate microstructure, having features of C-S as well as of C-Q.

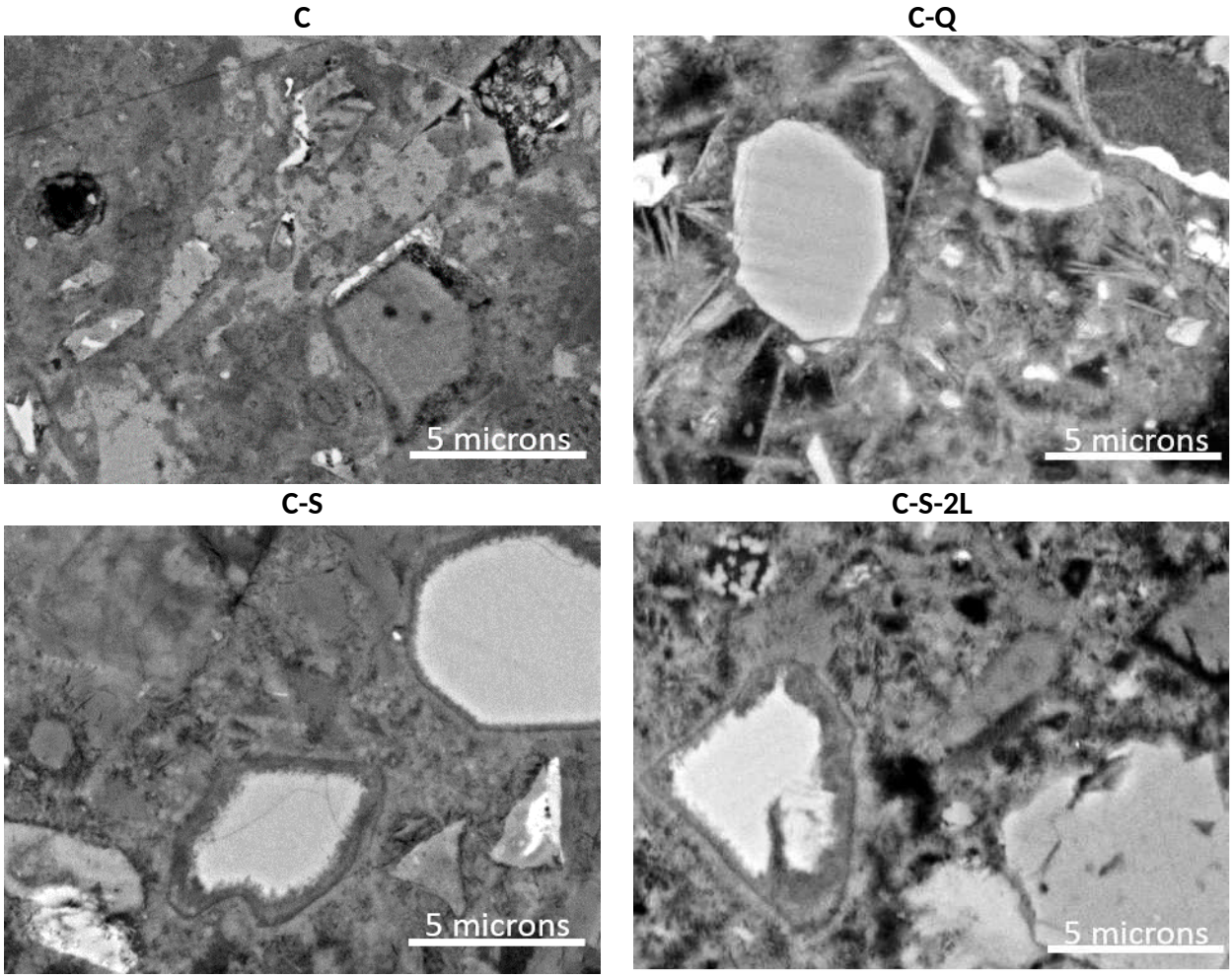

Figure 9 Microstructure of the samples cured for 180 days as seen by SEM-BSE.

In order to quantify the observed differences in porosity, the SEM-BSE micrographs were analyzed quantitatively using image analysis to determine the evolution in coarse capillary porosity [41].

The porosity evolution obtained by this method is shown in Figure 10. The porosity decreased with increased hydration time. It was lowest for the plain Portland cement and highest for the blend with quartz. The composite cements containing slag were similar and characterized by intermediate porosity levels.

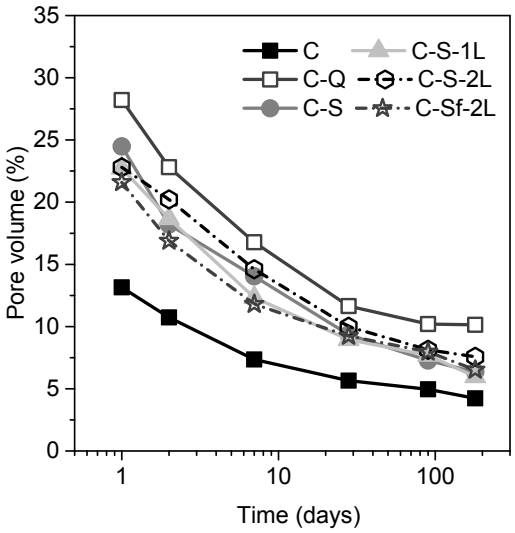

Figure 10 Pore volume evolution as measured by SEM-BSE. Results are averages from 50 images taken at 800x magnification and 2048∗1536 pixel resolution [30].

Additionally, MIP was used to study the pore volume evolution. The MIP technique was used to compare the porosity in the composite cements. This technique gives neither the absolute pore volume of the pores nor the pore size distribution, but can still be used as a comparative method [42] [43]. (Figure 11 and Figure 12). For all samples, the pore volume decreased with hydration time. The pore volume of the reference plain Portland cement was always lower than those of the corresponding composite cements and quartz reference, which was the highest, consistent with the SEM-BSE results. However, there were significant differences between both techniques. The pore volume determined by MIP was systematically higher than that determined by SEM-BSE, indicating that MIP can access a larger fraction of the total porosity.

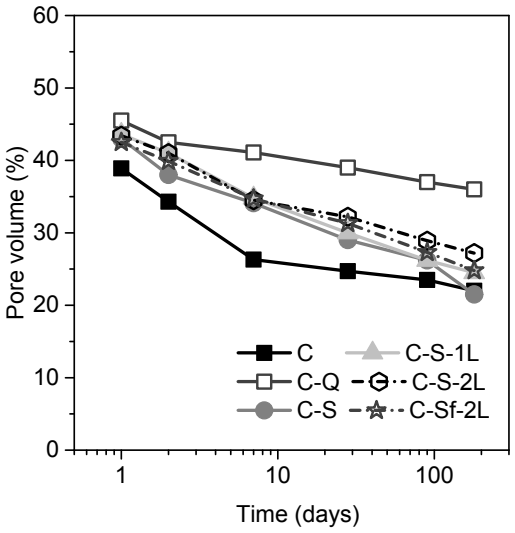

Figure 11 Pore volume as measured by MIP

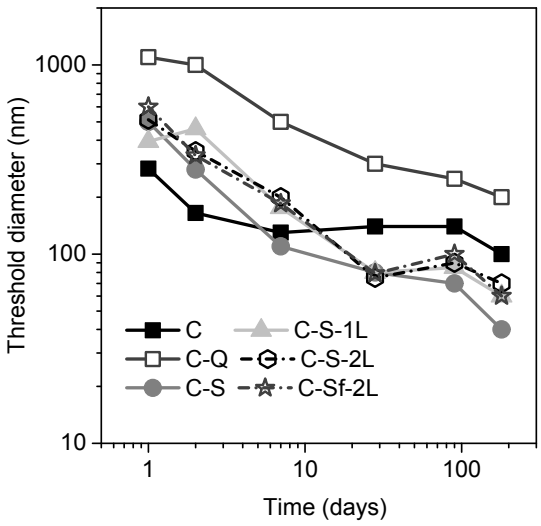

Figure 12 Threshold pore diameter from MIP data

To illustrate the effect of slag and limestone on pore structure, without taking time into account, plots were prepared of total intruded pore volume versus threshold pore size depicted in Figure 12, as performed in [44]. The results are shown in Figure 13. For composite cements, at later hydration times (7 days or below ca. 35 % porosity), the threshold pore diameter was measurably less in the composite cements than in the plain Portland cement paste with similar pore volume.

The porosity, calculated from the solid volume evolution, as determined by the hydration model GEMS, is shown in Figure 14. The calculated porosity includes the gel and capillary porosity, as well as chemical shrinkage, i.e. the reduction of the total volume of the system. The results showed the same trends as the data from SEM-BSE and MIP. The calculated total porosity volume was greater than that determined from the other methods.

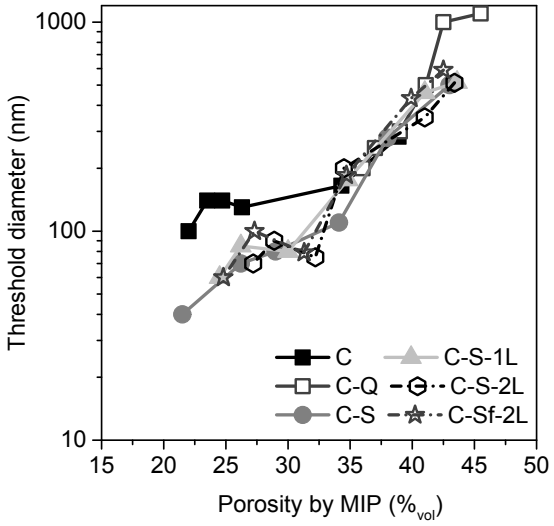

Figure 13: Relation between the threshold pore diameter and total porosity by MIP

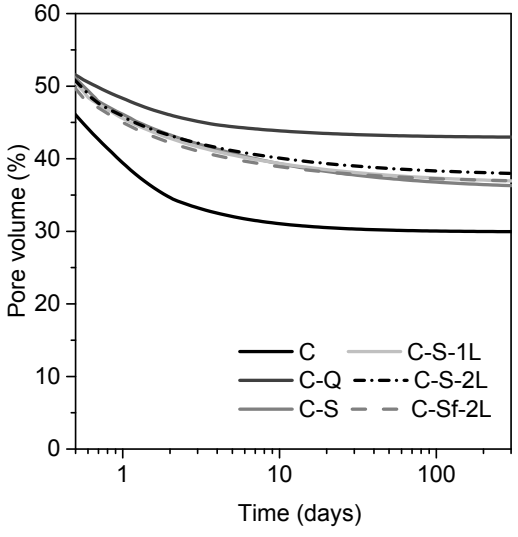

Figure 14: Pore volume evolution as calculated be the thermodynamic model

After 180 days, the mortar samples were analyzed for their water-accessible porosity, as described elsewhere [32]. Figure 15 shows the porosity partitioning according the saturation state at 95 % RH. The partitioning was obtained as follows. The dry fraction of porosity was obtained by the difference in weights of the samples stored at 95 % RH and after saturation. The saturated porosity was then calculated as the total porosity predicted by the GEMs model minus the dry porosity. To link the results collected at the mortar scale with those calculated at the paste level, a complete mass-volume balance was done as described in [31]. Figure 15 reveals that the fraction of dry porosity was much more sensitive to the binder type than the saturated fraction which stayed practically constant, at around 20 vol.-% of paste. The dry porosity ranged from ~10-% of paste in the case of sample C up to ~25 % for sample C-Q.

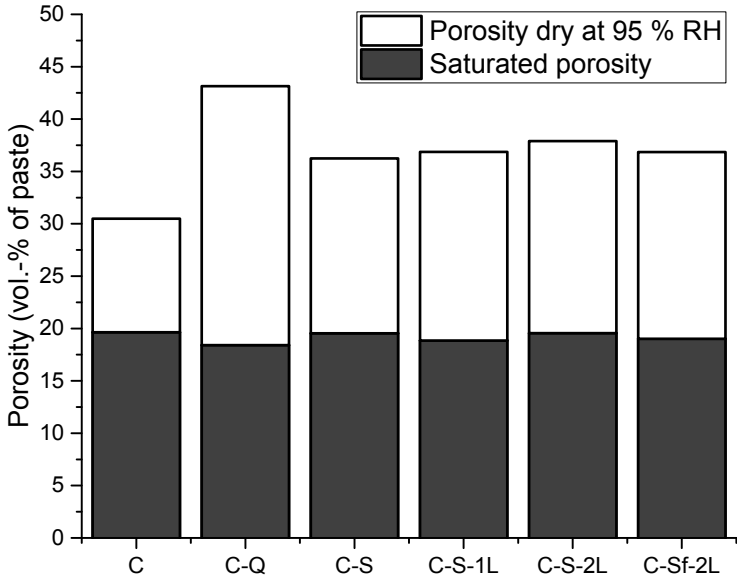

Figure 15: Partitioning of the porosity based on its saturation at 95 % RH. The total porosity modelled is sum of both parts. The representative error for the porosity fraction dry at 95 % RH (measured by the water porosity method) is estimated to ±1 vol.-% of paste.

4.5. Mechanical modeling

A micromechanical model has been applied to predict mortar performance by combining information about the volume of hydrates predicted by thermodynamic modelling and their spatial distribution, i.e. microstructure. The development of time-dependent volume fractions of selected mortars are shown in Figure 16. The figure highlights the porosity partitioning as well as the so-called C-S-H foam [23][24] which comprises the solid C-S-H and the saturated porosity. These two phases are homogenized at the first level of the micromechanical model and hence their volumes have the most pronounced impact on predicted performance. Our aim was to determine whether the model can correctly predict the differences in performance based on the differences in measured porosity and modelled hydrate assemblages.

The predicted compressive strengths and Young's moduli are compared with experimental data in Figure 17 and Figure 18, respectively. Generally, the predictions using the partitioned porosity matched favorably with experimental data, especially at later ages, i.e. when the porosity data were collected. At 1 and 2 days, modelling underestimated compressive strength and Young's modulus for the plain Portland cement.

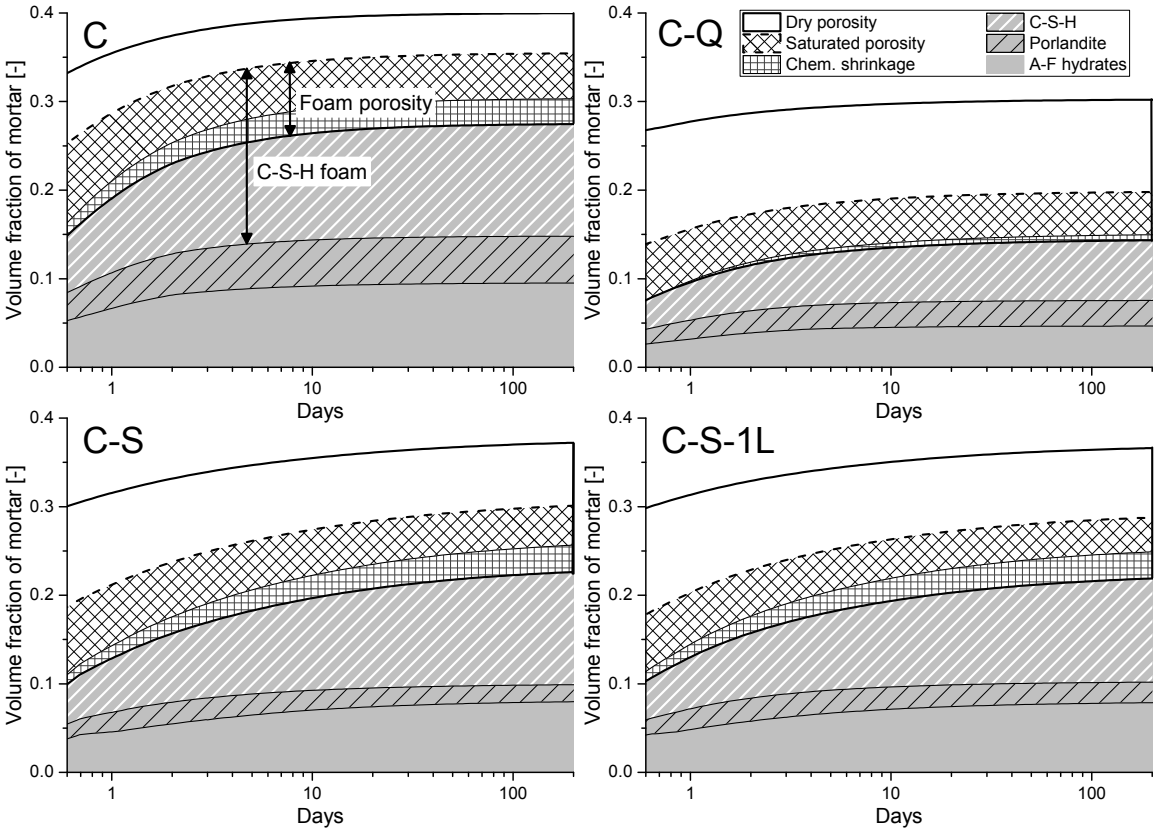

Figure 16: Evolution of time dependent volume fractions of selected mortars.

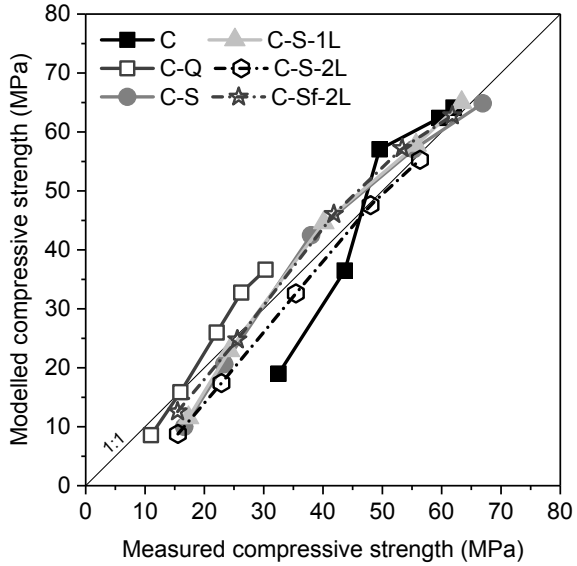

Figure 17 Comparison between measured and modelled compressive strength

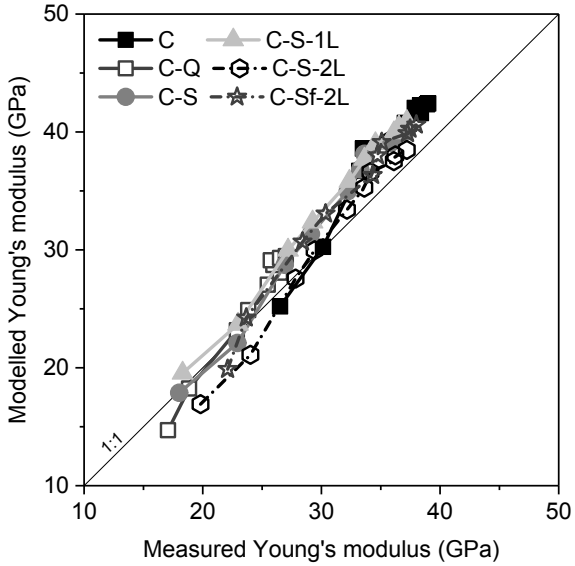

Figure 18 Comparison between measured and modelled Young's modulus

5. Discussion

5.1. Microstructure evolution

The three techniques used all provide different measures of porosity and hence allow analysis of pore volume and porosity distribution evolution and the impacts of SCMs:

- GEMS provides information on the total porosity, corresponding to that of the samples equilibrated at 11% relative humidity, i.e. including one monolayer of water on the C-S-H phase [17] [39] [45].
- MIP measures the accessible porosity to mercury up to a pressure of 400 MPa. This corresponds to a 4 nm pore diameter according to the Washburn–Laplace equation (assuming a contact angle of 140°)[42] [46]
- SEM-BSE image analysis measures coarse porosity. The theoretical minimum possible pore diameter measured corresponds to 0.34 µm (with a single pixel being 0.17 × 0.17 µm at the magnification used (800 ×), and assuming that the smallest visible pore corresponds to a 2x2 pixel feature). However, the practical minimum is greater than this due to the transition in grey level across pore-solid boundaries. Consequently only pores greater than approximatively 1 µm can be seen by this technique [47] [48].

Thus, while both experimental techniques probe only a part of the porosity, thermodynamic modelling provides the total porosity. A comparison of the results from these three techniques therefore enables an assessment of the microstructure and its evolution.

The MIP data show that the hydration of composite cements reduced the accessible porosity, plus the threshold pore diameter. In the case of the plain Portland cement, the threshold pore diameter changes little beyond 7 days. Hence, slag-containing binders have finer porosity for a given total porosity as shown in Figure 13. In another words, these binders have higher porosity volume for a given porosity fineness, which is in accordance with the literature data [44][49]. Contrary to [49], here presented results show a significant continuous microstructure refinement for composite cements. This might be associated with the higher w/b or longer hydration period used here. Indeed, the ongoing refinement of porosity over two years was reported in [44].

This impact of binder composition on microstructure development is further explored in Figure 19 and Figure 20 where the measured pore volumes by MIP and SEM are compared to the calculated total porosity by GEMS. All binders followed a similar trend. At higher porosities, i.e. at early ages, the predicted and measured porosities were similar. For higher hydration degrees, i.e. lower porosities, the measured pore volumes were lower than predicted. However, there was a significant difference between the plain Portland cement and the composite samples, including the quartz-bearing blend. In the composite cements, the measured pore volume was significantly lower for any given calculated volume, compared to the plain Portland cement paste. It is noticeable that the quartz-containing sample behaved like the slag-containing binders and did not follow the trend of the C sample. These results show that the arrangement of hydrates in space is different. For a given total porosity, the composite cements were characterized by lower MIP-accessible porosity. Given the fact that pores are only accessible to mercury during MIP if they are connected to the bulk porosity by pores larger than 4 nm, this implies that the composite cements contain a higher volume of pores below this size. Hence, for a given total pore volume, the content of pores larger than 4 nm is lower in the composite cements compared to the plain Portland cement.

The same conclusion can be drawn when comparing the total calculated porosity to the porosity measured by SEM-BSE, as shown in Figure 20. For the higher hydration degree, corresponding to a measured pore volume less than 15 %, the composite cements possessed higher pore volumes comprising small pores not visible by SEM-BSE. At the same time, the volume of large pores is lower

than that of plain Portland cement with the same total porosity. Interestingly, unlike with the MIP data shown in Figure 19, SEM-BSE imaging revealed a difference between the composite cements and the quartz-bearing blend. The latter possessed a more refined porosity than the slag containing samples, evidenced by the lower measured pore volume for a given calculated pore volume.
This phenomenon, evident in the composite cements, is frequently called more efficient space filling [49] by hydrates. The efficiency is related to the ability to reduce the coarse porosity, since it is believed to be the main driver of the compressive strength of paste.

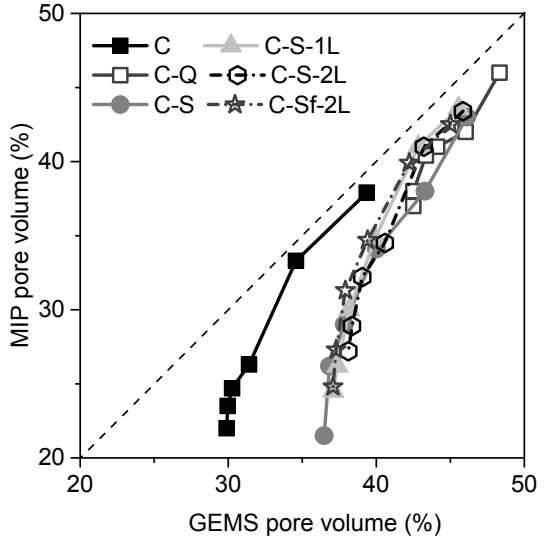

Figure 19 Comparison of porosity as calculated from GEMS and measured by MIP. The lines are only guides for the eye.

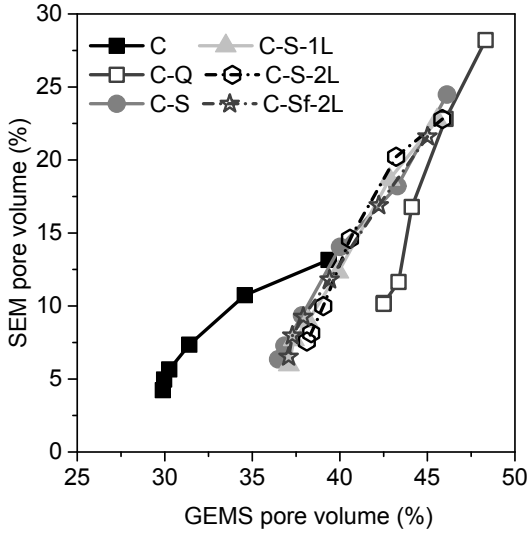

Figure 20 Comparison of porosity as calculated from GEMS and measured by SEM-BSE. The lines are only guides for the eye.

The differences in the microstructures of the investigated samples correlate well with the difference of the C-S-H phase composition as shown in [30]. Therefore, the next paragraphs focus on the C-S-H phase since its morphology is variable and depends on the binder composition. Other hydrates are crystalline, i.e. ettringite, portlandite, AFm phases and hydrogarnets. Their morphology is much better defined and constant compared to the C-S-H [50]. One notes that hydrotalcite can be XRD amorphous and of variable composition [16]; however it is present in significantly lower quantities than is the C-S-H (Figure 6). Hence, the impacts of these crystalline phases are accurately included in the total solid volume predicted by GEMs.
The differences in chemical composition of the binders is reflected in the C–S–H composition, which had lower Ca/Si and higher Al/Si ratios in the composite cements than in the plain Portland cement pastes [30] [3] [51]. These modifications in the C–S–H composition have been associated with a change in morphology, from fibrillar to foil-like with decreasing Ca/Si [52] [53] [54]. However, the chemical composition of the reactive components of C and C-Q binders (i.e. excluding the inert quartz) was identical. Yet, the microstructure develops (densifies) distinctly differently. Work of Chaussadent [55] and later Muller [56] showed that higher water to binder ratios lead to lower Ca/Si in the C-S-H. This is confirmed with this work as well as shown in Table 5 where samples with w/b of 0.5 and effective w/c of 0.5 and 1, respectively, are compared. The density of porous C–S–H, including the gel water decreases with increasing water to binder ratio [56].

Table 5 Ca/Si ratio of C-S-H in the C and C-Q sample by SEM-EDS

Sample	180 days
C (w/b=0.5, w/c=0.5)	1.81

C-Q (w/b=0.5, w/c=1)	1.49

Consequently, the change of the bulk chemical composition as well as the increase of water to binder ratio may lead to the modification of the properties and distribution of C-S-H phase and consequent distribution of the hydrates.

It is important to notice that the model calculated the same density of the solid C-S-H in all investigated samples. Nevertheless, this is reported to be constant at different water to binder ratios [56] and with silica fume [57] at later hydration time. Additionally, it was shown that the Al incorporation into the C-S-H does not alter its physical properties [58]. This further supports validity of our model.

5.1. Correlation between pore volume and strength

It is generally accepted that the mechanical performance of cements depends on their pore volume and its distribution [59]. The aforementioned discussion confirmed that the microstructure of the plain Portland and composite cements is different. Below, a discussion follows if, and how, different measured and calculated pore volumes relate to the performance.

Figure 21 and Figure 22 show the relationship between the pore volumes determined by SEM and MIP, respectively, and compressive strength. As expected, lower porosities result in higher strengths. However, both relationships have a significant scatter. For a given measured porosity, the strength can vary by more than 20 MPa. Hence, these relationships are not capable of discriminating the individual binders. Similar findings and conclusions have been reported elsewhere [60] .

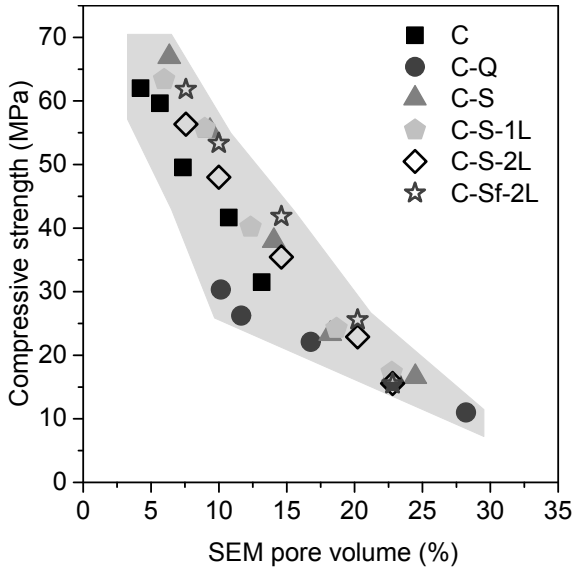

Figure 21 Comparison of compressive strength and pore volume measured by SEM-BSE. The gray area highlights the scatter of data points.

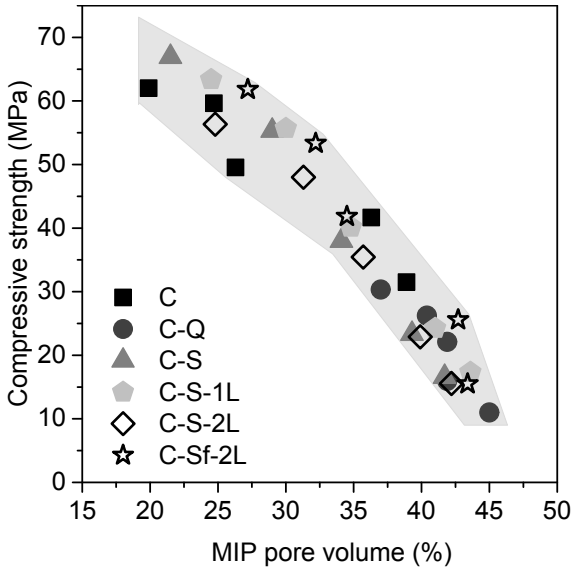

Figure 22 Comparison of compressive strength and pore volume measured by MIP. The gray area highlights the scatter of data points.

Application of the third technique, thermodynamic modelling, is shown in Figure 23 and Figure 24 comparing compressive strength, Young's modulus and calculated porosity by GEMS; i.e. total porosity in the investigated pastes. Again, both mechanical properties scale with porosity, which is, in turn, inversely proportional to the overall hydration degree. However, the graphs reveal that there is no unique relationship between the porosity and mechanical properties. Particularly at later times, i.e. at lower porosities, for a given pore volume, the composite cements were characterized by better

performance for a given pore volume. The same conclusion could be drawn when comparing the evolution of mechanical properties with the bound water content, as shown in Figure 4.

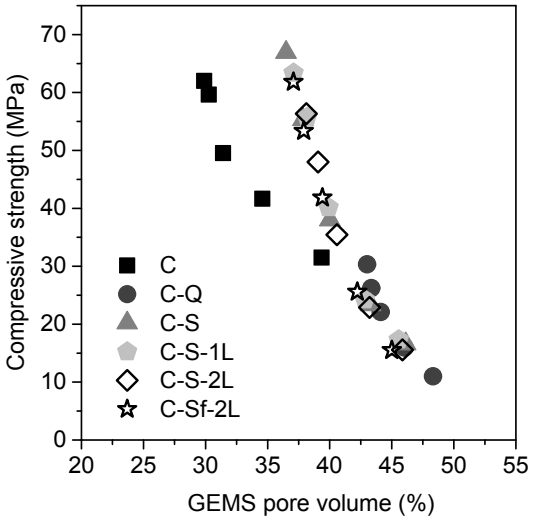

Figure 23 Comparison between measured compressive strength and calculated porosity volume by GEMS

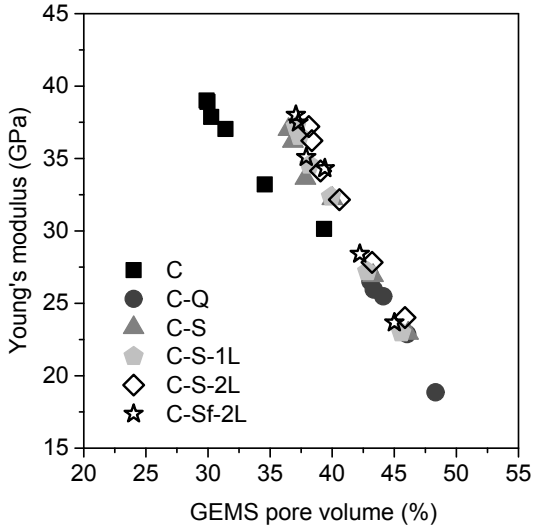

Figure 24 Comparison between measured Young's modulus and calculated porosity volume by GEMS

In literature, the relationship between the calculated total porosity and strength was corrected by adjusting the density of C-S-H [16] [17] [21] [61] [62]. Figure 25 and Figure 26 show the results of such an approach. The C-S-H densities were fitted to yield a unique relationship. The density of C-S-H in the composite cements was decreased to 2.0 g/cm^3 while it was kept as given by GEMs, i.e. at 2.4 g/cm^3, in the plain Portland cement paste. This concept reflects the better filling capacity of the composite cements discussed in the previous paragraph.

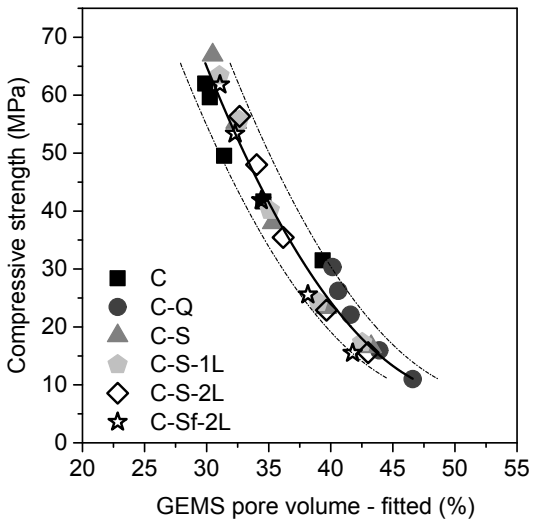

Figure 25 Comparison between measured compressive strength and porosity volume calculated by GEMS. The density of C-S-H in composite cements including C-Q

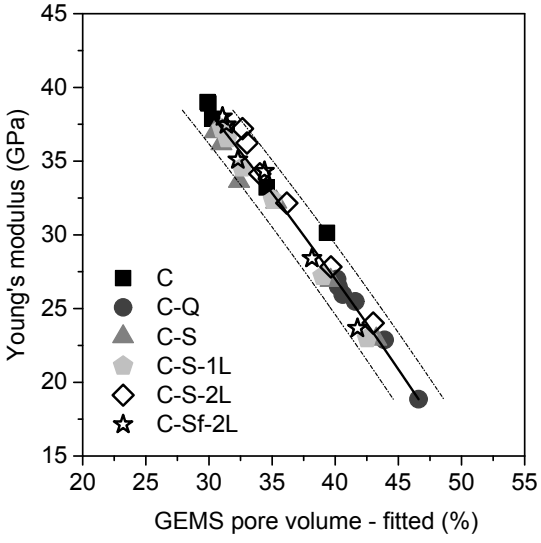

Figure 26 Comparison between measured Young's modulus and calculated porosity volume by GEMS. The density of C-S-H in composite cements including C-Q

was adjusted. Cubic fit is shown with bounds of ± 2 % pore volume; this corresponds roughly to the change of hydration degree of slag of 5 %.

was adjusted. Cubic fit is shown with bounds of ± 2 % pore volume; this corresponds roughly to the change of hydration degree of slag of 5 %.

However, the adjustments of C-S-H density are not supported by the latest data published in the literature. The apparent density of C-S-H, Muller called it as the bulk C-S-H density, is similar for plain Portland cement and cement blended with silica fume [56][57]. These findings do not substantiate why the fitting parameter (i.e. the density correction) for the plain Portland cement and composite cements should be different.

The relationship in Figure 25, despite being unique, does not offer any explanation for the differences observed between the binders. The correlation between fitted porosity and strength does not imply causation since the relationship is free of any underlying mechanisms. Consequently, it is impossible to judge whether the differences in microstructure discussed above are relevant for the mechanical performance evolution. This is consistent with the statement of Taylor in 1990 that "strength cannot be explained by relating it empirically to porosity or pore size distribution; it is necessary to know what holds the material together and what happens when it fails" [59]. The micromechanical model, on the other side, includes the failure criterion as well as distinguishes contributions of different phases at different scale to the performance. This enables studying mechanisms responsible for the differences in performance observed.

5.2. Insights from micromechanical model

When assuming that the mechanical properties and density of the solid C-S-H depend little on the cement composition [58] [63] [57], the higher strength of the composite cements measured at later ages despite their lower bound water contents and higher porosities needs to be explained by a different spatial arrangement of the hydrates, i.e. by differences in microstructure. Therefore, a micromechanical model was applied, which explicitly considered the spatial arrangement of hydrates and porosity. Additionally, it contained an explicit failure mechanism which made it suitable to study the impact of microstructure on performance.

As described in Section 3.3, the micromechanical model consisted of three homogenization levels of mechanical properties. The first level at the smallest length scale included the solid C-S-H and the saturated porosity fraction. This level is schematically highlighted as the C-S-H foam in Figure 16 for sample C. The saturated porosity at the mortar level was measured by the water porosity method. By comparing the weights of samples equilibrated at 95 % RH which were subsequently saturated, the volume of dry pores was accurately determined. The difference in the volume of the total porosity predicted by the thermodynamic model and the dry porosity was assumed to be saturated. The dry porosity was assigned to the second homogenization step.

Figure 27 shows the calculated porosity of the C-S-H foam, Figure 28 the volume of the foam and Figure 29 the volume of the remaining, i.e. dry, part of porosity. In these figures, the volumes are expressed per 100 g of binder to facilitate the comparison against previous results.

The calculated dry porosity development is shown in Figure 29. The development was based on the assumption that the fraction of the total and coarse porosity was constant over time and equal to that measured at 180 days. The general trends, as well as values, were comparable to the SEM-BSE data presented in Figure 10. However, this evolution did not correlate with the evolution of mechanical performance. At 180 days, the strengths of the plain Portland cement and slag-bearing samples were comparable, but their calculated coarse porosities differed by a factor of two. To explain this discrepancy, the level of C-S-H foam was analyzed in detail and its impact on overall mechanical performance determined.

Figure 27 and Figure 28 are related to the amount of binding phase (C-S-H foam) present and its properties. The volume of foam increased over time, as more C-S-H was formed and the porosity is refined. The densification of the foam and its similar density after 180 days are in agreement with the experimental data from Muller [56] [57]. The development of foam volume resembles the development of mechanical performance. However, the foam volume alone cannot explain the higher strength of composite cements when compared to the plain Portland cement after 180 days. The foam porosity is shown in Figure 27. It decreased rapidly in the case of the plain Portland cement. For the composite cements, the decrease was slower at early age, but continued for a longer period. The final foam porosities of C-S, C-S-1L and C-Sf-2L were comparable, or even lower, than that of the plain Portland cement.

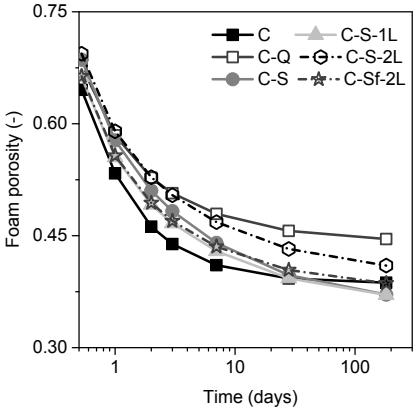

Figure 27 Calculated C-S-H foam porosity

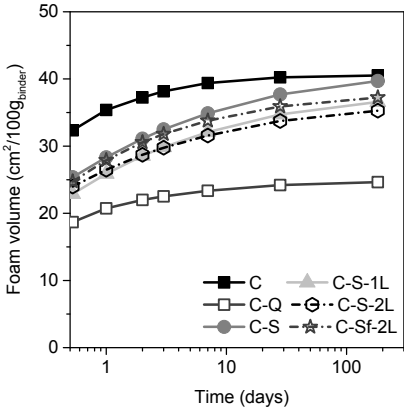

Figure 28 Calculated C-S-H foam volume

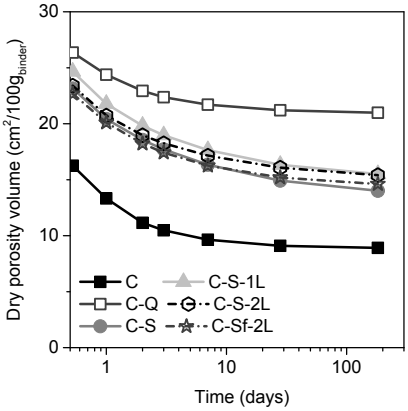

Figure 29: Calculated dry porosity volume.

5.2.1.Effect of the C-S-H foam

The importance of the amount of foam and its densification is further explored in Figure 30, showing a simplified scenario consisting of two homogenization levels and three phases: solid C-S-H, foam porosity and coarse (dry) porosity. The first level included the solid C-S-H and foam porosity and was homogenized using the self-consistent method, identically to the modelling framework applied. The second level included the homogenized C-S-H foam and the coarse porosity. The porosity distribution between the coarse, i.e. at the second level, and the fine as well as the total porosity were varied. Note that in this simplified case, the total porosity is reversibly proportional to the volume of the solid C-S-H. The results demonstrate that the sensitivity of the resulting matrix strength to total porosity significantly increased with increasing coarse porosity, i.e. less foam porosity. In another words, for a given total porosity, i.e. for a given solid C-S-H volume, the higher is the coarse porosity, the higher is the strength.

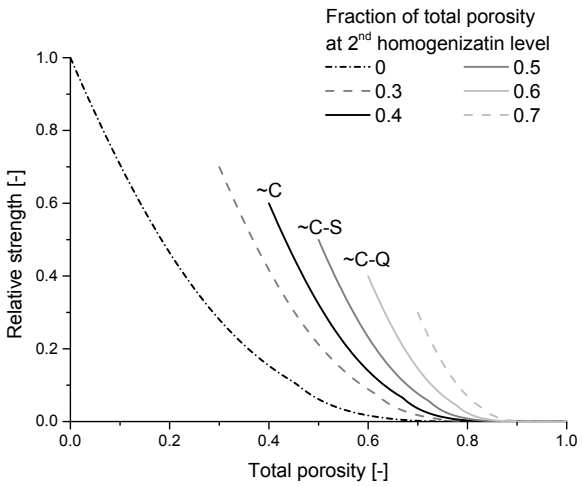

Figure 30: Impact of porosity distribution into two different homogenization levels on the resulting strength of the matrix. The highlighted lines approximately correspond to the experimentally determined distributions of porosity by the water porosity method at 180 days.

This analysis suggests that C-S-H foam densification and an increase in foam content can explain the experimentally observed differences in compressive strength development. For a given volume of hydrates formed, i.e. total porosity filled, more hydrates are formed at the scale of the foam in the case of composite cements compared to the Portland cement. Such porosity reduction is, as demonstrated in Figure 30, significantly more efficient with respect to mechanical performance.

The micromechanical model reflects microstructure of binders in two ways. The first way is the distribution of phases to different homogenization levels. This distribution is given by the physical size of the phases and is constant for all binders. The second way is the porosity partitioning based on the water saturation. Applying Kelvin-Laplace relationship with surface tension of 0.073 N/m [64], 95 % RH humidity corresponds to an entry pore diameter of about 40 nm. Comparing the MIP data at later ages (c.f. Figure 13) shows that while the MIP pore volume of the plain Portland cement reduced, the threshold pore diameter did not change significantly. In the case of composite cements, the porosity reduction was accompanied by its refinement at the scale of tens nm as demonstrated by the MIP data. This results in denser, stronger, foam and hence leads to higher strengths. It also implies that the volume of total porosity, without knowing its porosity distribution, cannot be used as the single parameter for strength prediction. Such findings are consistent with the MIP data presented elsewhere [49].

5.2.2.Effect of other hydrates

Contrary to the hypothetical example from Figure 30, the hydrate assemblages studied here contain other hydrates in addition to C-S-H. The volume of these hydrates is predicted by the thermodynamic model. By the micromechanical model setup, these hydrates contribute to the performance by reducing the coarse porosity at the second homogenization level. Consequently, an increase in their volume results in a strength increase. At later ages, this increase is more pronounced for composite cements since their foam is denser. In reality, however, the impact of these other hydrates cannot be taken separately from the impact of the C-S-H foam. Since all hydrates including the C-S-H precipitate simultaneously and at the same space, they will mutually influence each other. This might change the porosity distribution and hence the foam properties and volume. In another words, the other hydrates might force the C-S-H to form in confined space leading to enhanced foam densification.

5.3. Effect of limestone

Limestone enhances the kinetics of slag reaction and impacts hydrates assemblages (c.f. Figure 3 and Figure 5). This study reveals that the enhanced kinetics is the dominant parameter among those investigated. The faster reaction of the slag compensates for its lower content when compared to the slag cement without limestone addition. This leads to formation of relatively more C-S-H foam, accompanied by formation of other hydrates such as AFm. Additionally, the reactive carbonates impact the alumina redistribution which further increases the AFm content. All these changes are reflected by the modelling framework applied, i.e. the thermodynamic and micromechanical model, which then leads to accurate performance prediction, even for limestone containing binders.

6. Conclusions

Hydration of Portland-slag-limestone composite cements and investigated relationships between their porosity, microstructure and performance were studied and quantified. The investigations included different experimental techniques as well as a modelling framework comprising a thermodynamic model for phase assemblage development incorporated into a micromechanical model for mortar performance.

The various techniques and analyses of microstructure confirmed the differences between the plain Portland and composite cements pates, i.e. the refined microstructure. The quartz-containing composite cement behaved similarly to the slag-containing composite cements. The same trends in microstructure evolution were observed by the SEM and MIP techniques despite their different resolutions and measurement principles.

Two approaches linking the mechanical performance with microstructure were investigated. The simple relationship between the calculated total porosity and mortar strengths required C-S-H density correction factor to provide a unique relationship for plain Portland as well as composite cements. This approach, however, is not consistent with the latest NMR data on C-S-H composition. Additionally, it does not allow identification and study of the differences between composite and plain Portland cements.

Therefore, a micromechanical model with explicit spatial arrangement of hydrates and porosity partitioned into coarse and fine fraction, based on its saturation, was applied. The model revealed and quantified that the different porosity distribution between the composite and plain Portland cements is responsible for the higher strength of composite cements despite their higher total porosity. At later ages, the hydration of slag results in formation of a microstructure more efficient for compressive strength and elastic stiffness. The hydrates formed lead not only to porosity filling, but also to microstructure refinement at the scales below tens of nm. In the plain Portland cement, only porosity filling takes place. This is consistent with general trends of MIP and NMR. Using the modelling framework developed, the aforementioned phenomena could be quantified. Nevertheless, the origin of the differences in the microstructure development is still not fully recognized.

Limestone, in the ternary systems investigated, improves the strength development in two ways: it accelerates the slag hydration and modifies hydrate assemblage. This leads to more efficient microstructure for performance evolution resulting in performance comparable to limestone free binary systems.

Acknowledgement

This work was funded by the University of Leeds and HeidelbergCement Technology Centre.

7. Literature

[1] H. Klee, “The cement sustainability initiative,” in *PROCEEDINGS-INSTITUTION OF CIVIL ENGINEERS ENGINEERING SUSTAINABILITY*, 2004, vol. 157, pp. 9–12.

[2] L. Barcelo, J. Kline, G. Walenta, and E. Gartner, “Cement and carbon emissions,” *Mater. Struct.*, vol. 47, no. 6, pp. 1055–1065, 2014.

[3] B. Lothenbach, K. Scrivener, and R. D. Hooton, “Supplementary cementitious materials,” *Cem. Concr. Res.*, vol. 41, no. 12, pp. 1244–1256, 2011.

[4] K. L. Scrivener, P. Juilland, and P. J. M. Monteiro, “Advances in understanding hydration of Portland cement,” *Cem. Concr. Res.*, Jun. 2015.

[5] P. T. Durdziński, R. Snellings, C. F. Dunant, M. B. Haha, and K. L. Scrivener, “Fly ash as an assemblage of model Ca–Mg–Na-aluminosilicate glasses,” *Cem. Concr. Res.*, vol. 78, pp. 263–272, Dec. 2015.

[6] M. Alexander and M. Thomas, “Service life prediction and performance testing — Current developments and practical applications,” *Cem. Concr. Res.*, vol. 78, pp. 155–164, Dec. 2015.

[7] R. Douglas Hooton, “Current developments and future needs in standards for cementitious materials,” *Cem. Concr. Res.*, vol. 78, pp. 165–177, Dec. 2015.

[8] J. S. Dolado and K. van Breugel, “Recent advances in modeling for cementitious materials,” *Cem. Concr. Res.*, vol. 41, no. 7, pp. 711–726, Jul. 2011.

[9] D. Damidot, B. Lothenbach, D. Herfort, and F. P. Glasser, “Thermodynamics and cement science,” *Cem. Concr. Res.*, vol. 41, no. 7, pp. 679–695, Jul. 2011.

[10] B. Lothenbach, G. Le Saout, E. Gallucci, and K. Scrivener, “Influence of limestone on the hydration of Portland cements,” *Cem. Concr. Res.*, vol. 38, no. 6, pp. 848–860, Jun. 2008.

[11] M. Whittaker, M. Zajac, M. Ben Haha, F. Bullerjahn, and L. Black, “The role of the alumina content of slag, plus the presence of additional sulfate on the hydration and microstructure of Portland cement-slag blends,” *Cem. Concr. Res.*, vol. 66, pp. 91–101, Dec. 2014.

[12] A. Schöler, B. Lothenbach, F. Winnefeld, and M. Zajac, “Hydration of quaternary Portland cement blends containing blast-furnace slag, siliceous fly ash and limestone powder,” *Cem. Concr. Compos.*, vol. 55, pp. 374–382, Jan. 2015.

[13] M. Zajac, S. K. Bremseth, M. Whitehead, and M. Ben Haha, “Effect of CaMg(CO3)2 on hydrate assemblages and mechanical properties of hydrated cement pastes at 40°C and 60°C,” *Cem. Concr. Res.*, vol. 65, pp. 21–29, Nov. 2014.

[14] M. Antoni, J. Rossen, F. Martirena, and K. Scrivener, “Cement substitution by a combination of metakaolin and limestone,” *Cem. Concr. Res.*, vol. 42, no. 12, pp. 1579–1589, Dec. 2012.

[15] M. Zajac, A. Rossberg, G. Le Saout, and B. Lothenbach, “Influence of limestone and anhydrite on the hydration of Portland cements,” *Cem. Concr. Compos.*, vol. 46, pp. 99–108, Feb. 2014.

[16] Kucharczyk Sylwia, Deja Jan, and Maciej Zajac, “Effect of slag reactivity influenced by alumina content on hydration of composite cements,” *J. Adv. Concr. Technol.*, vol. 4, pp. 535–547, 2016.

[17] B. Lothenbach, T. Matschei, G. Möschner, and F. P. Glasser, “Thermodynamic modelling of the effect of temperature on the hydration and porosity of Portland cement,” *Cem. Concr. Res.*, vol. 38, no. 1, pp. 1–18, Jan. 2008.

[18] B. Lothenbach and F. Winnefeld, “Thermodynamic modelling of the hydration of Portland cement,” *Cem. Concr. Res.*, vol. 36, no. 2, pp. 209–226, Feb. 2006.

[19] K. De Weerdt, M. B. Haha, G. Le Saout, K. O. Kjellsen, H. Justnes, and B. Lothenbach, “Hydration mechanisms of ternary Portland cements containing limestone powder and fly ash,” *Cem. Concr. Res.*, vol. 41, no. 3, pp. 279–291, Mar. 2011.

[20] B. Lothenbach, G. Le Saout, M. B. Haha, R. Figi, and E. Wieland, “Hydration of a low-alkali CEM III/B–SiO 2 cement (LAC),” *Cem. Concr. Res.*, vol. 42, no. 2, pp. 410–423, 2012.

[21] M. Zajac and M. Ben Haha, “Experimental investigation and modeling of hydration and performance evolution of fly ash cement,” *Mater. Struct.*, vol. 47, no. 7, pp. 1259–1269, Jul. 2014.

[22] B. Pichler *et al.*, “Effect of gel-space ratio and microstructure on strength of hydrating cementitious materials: An engineering micromechanics approach,” *Cem. Concr. Res.*, vol. 45, 2013.
[23] B. Pichler and C. Hellmich, “Upscaling quasi-brittle strength of cement paste and mortar: A multi-scale engineering mechanics model,” *Cem. Concr. Res.*, vol. 41, no. 5, pp. 467–476, May 2011.
[24] P. Termkhajornkit, Q. H. Vu, R. Barbarulo, S. Daronnat, and G. Chanvillard, “Dependence of compressive strength on phase assemblage in cement pastes: Beyond gel–space ratio — Experimental evidence and micromechanical modeling,” *Cem. Concr. Res.*, vol. 56, pp. 1–11, Feb. 2014.
[25] J. Sanahuja, L. Dormieux, and G. Chanvillard, “Modelling elasticity of a hydrating cement paste,” *Cem. Concr. Res.*, vol. 37, no. 10, pp. 1427–1439, Oct. 2007.
[26] B. Pichler, S. Scheiner, and C. Hellmich, “From micron-sized needle-shaped hydrates to meter-sized shotcrete tunnel shells: micromechanical upscaling of stiffness and strength of hydrating shotcrete,” *Acta Geotech.*, vol. 3, no. 4, pp. 273–294, Dec. 2008.
[27] C. Pichler, R. Lackner, and H. A. Mang, “A multiscale micromechanics model for the autogenous-shrinkage deformation of early-age cement-based materials,” *Eng. Fract. Mech.*, vol. 74, no. 1–2, pp. 34–58, Jan. 2007.
[28] C. Pichler and R. Lackner, “A multiscale creep model as basis for simulation of early-age concrete behavior,” *Comput. Concr.*, vol. 5, no. 4, pp. 295–328, 2008.
[29] Q. H. Vu, E. Guillon, G. Chanvillard, and R. Barbarulo, “A HOMOGENIZATION METHOD TO MODEL THE COMPRESSIVE STRENGTH OF LIGHTWEIGHT AGGREGATE CONCRETE.” .
[30] S. Adu-Amankwah, M. Zajac, C. Stabler, M. Ben Haha, and L. Black, “Influence of limestone on the hydration of ternary slag cement,” *Cem. Concr. Res.*, Volume 100, October 2017, Pages 96-109.
[31] J. Skocek, M. Zajac, C. Stabler, and M. Ben Haha, “Predictive modelling of hydration and mechanical performance of low Ca composite cements: possibilities and limitations from industrial perspective,” *Cem. Concr. Res.*, Volume 100, October 2017, Pages 68-83.
[32] SIA, “Betonbau – Ergänzende Festlegungen 262/1.” SIA Zurich, 2003.
[33] D. A. Kulik *et al.*, “GEM-Selektor geochemical modeling package: revised algorithm and GEMS3K numerical kernel for coupled simulation codes,” *Comput. Geosci.*, vol. 17, no. 1, pp. 1–24, 2013.
[34] T. Wagner, D. A. Kulik, F. F. Hingerl, and S. V. Dmytrieva, “GEM-Selektor geochemical modeling package: TSolMod library and data interface for multicomponent phase models,” *Can. Mineral.*, vol. 50, no. 5, pp. 1173–1195, 2012.
[35] W. Hummel, U. Berner, E. Curti, F. Pearson, and T. Thoenen, “Nagra/PSI chemical thermodynamic data base 01/01,” *Radiochim. Acta*, vol. 90, no. 9–11/2002, pp. 805–813, 2002.
[36] W. Hummel, U. Berner, E. Curti, F. Pearson, and T. Thoenen, “Nagra Technical Report NTB 02-16,” *Wettingen Switz.*, 2002.
[37] “Empa - 308 - Concrete / Construction Chemistry - Services.” [Online]. Available: https://www.empa.ch/web/s308/cemdata. [Accessed: 05-Oct-2016].
[38] T. Matschei, B. Lothenbach, and F. P. Glasser, “Thermodynamic properties of Portland cement hydrates in the system CaO–Al2O3–SiO2–CaSO4–CaCO3–H2O,” *Cem. Concr. Res.*, vol. 37, no. 10, pp. 1379–1410, Oct. 2007.
[39] D. A. Kulik, “Improving the structural consistency of CSH solid solution thermodynamic models,” *Cem. Concr. Res.*, vol. 41, no. 5, pp. 477–495, 2011.
[40] V. Kocaba, E. Gallucci, and K. L. Scrivener, “Methods for determination of degree of reaction of slag in blended cement pastes,” *Cem. Concr. Res.*, vol. 42, no. 3, pp. 511–525, Mar. 2012.
[41] K. L. Scrivener, “Backscattered electron imaging of cementitious microstructures: understanding and quantification,” *Cem. Concr. Compos.*, vol. 26, no. 8, pp. 935–945, Nov. 2004.
[42] S. Diamond, “Mercury porosimetry: an inappropriate method for the measurement of pore size distributions in cement-based materials,” *Cem. Concr. Res.*, vol. 30, no. 10, pp. 1517–1525, 2000.

[43] C. Gallé, “Effect of drying on cement-based materials pore structure as identified by mercury intrusion porosimetry: a comparative study between oven-, vacuum-, and freeze-drying,” *Cem. Concr. Res.*, vol. 31, no. 10, pp. 1467–1477, 2001.
[44] “Canut - Impact of curing on the porosity development of cement pastes with and without slag - 2011.pdf.” .
[45] H. M. Jennings, “Refinements to colloid model of C-S-H in cement: CM-II,” *Cem. Concr. Res.*, vol. 38, no. 3, pp. 275–289, Mar. 2008.
[46] C. Galle, “Effect of drying on cement-based materials pore structure as identified by mercury intrusion porosimetry: a comparative study between oven-, vacuum-, and freeze-drying,” *Cem. Concr. Res.*, vol. 31, no. 10, pp. 1467–1477, 2001.
[47] M. H. N. Yio, H. S. Wong, and N. R. Buenfeld, “3D Monte Carlo simulation of backscattered electron signal variation across pore-solid boundaries in cement-based materials,” *Cem. Concr. Res.*, vol. 89, pp. 320–331, Nov. 2016.
[48] M. B. Haha, K. De Weerdt, and B. Lothenbach, “Quantification of the degree of reaction of fly ash,” *Cem. Concr. Res.*, vol. 40, no. 11, pp. 1620–1629, Nov. 2010.
[49] E. Berodier and K. Scrivener, “Evolution of pore structure in blended systems,” *Cem. Concr. Res.*, vol. 73, pp. 25–35, Jul. 2015.
[50] H. F. Taylor, *Cement chemistry*. Thomas Telford, 1997.
[51] I. G. Richardson, “The calcium silicate hydrates,” *Cem. Concr. Res.*, vol. 38, no. 2, pp. 137–158, Feb. 2008.
[52] R. Taylor, I. G. Richardson, and R. M. D. Brydson, “Composition and microstructure of 20-year-old ordinary Portland cement–ground granulated blast-furnace slag blends containing 0 to 100% slag,” *Cem. Concr. Res.*, vol. 40, no. 7, pp. 971–983, Jul. 2010.
[53] J. E. Rossen, B. Lothenbach, and K. L. Scrivener, “Composition of C–S–H in pastes with increasing levels of silica fume addition,” *Cem. Concr. Res.*, vol. 75, pp. 14–22, 2015.
[54] E. Tajuelo Rodriguez, I. G. Richardson, L. Black, E. Boehm-Courjault, A. Nonat, and J. Skibsted, “Composition, silicate anion structure and morphology of calcium silicate hydrates (C-S-H) synthesised by silica-lime reaction and by controlled hydration of tricalcium silicate (C_3S),” *Adv. Appl. Ceram.*, vol. 114, no. 7, pp. 362–371, Oct. 2015.
[55] T. Chaussadent, V. Baroghel-Bouny, H. Hornain, N. Rafaï, and A. Ammouche, “Effect of water-cement ratio of cement pastes on microstructural characteristics related to carbonation process,” *Spec. Publ.*, vol. 192, pp. 523–538, 2000.
[56] A. C. Muller, K. L. Scrivener, A. M. Gajewicz, and P. J. McDonald, “Densification of C–S–H measured by 1H NMR relaxometry,” *J. Phys. Chem. C*, vol. 117, no. 1, pp. 403–412, 2012.
[57] A. C. A. Muller, K. L. Scrivener, J. Skibsted, A. M. Gajewicz, and P. J. McDonald, “Influence of silica fume on the microstructure of cement pastes: New insights from 1H NMR relaxometry,” *Cem. Concr. Res.*, vol. 74, pp. 116–125, Aug. 2015.
[58] J. E. Oh, S. M. Clark, and P. J. M. Monteiro, “Does the Al substitution in C–S–H(I) change its mechanical property?,” *Cem. Concr. Res.*, vol. 41, no. 1, pp. 102–106, Jan. 2011.
[59] H. F. Taylor, *Cement Chemistry*. .
[60] X. Zhang, “Quantitative microstructural characterisation of concrete cured under realistic temperature conditions,” Ecole Polytechnique Fédérale de Lausanne, Lausanne, 2007.
[61] P. Termkhajornkit and T. Nawa, “Composition of CSH in the Hydration Products of Fly Ash-Cement System,” *Spec. Publ.*, vol. 242, pp. 361–374, 2007.
[62] T. Ishida, Y. Luan, T. Sagawa, and T. Nawa, “Modeling of early age behavior of blast furnace slag concrete based on micro-physical properties,” *Cem. Concr. Res.*, vol. 41, no. 12, pp. 1357–1367, 2011.

[63] A. C. A. Muller, “Characterization of porosity & CSH in cement pastes by 1H NMR,” ÉCOLE POLYTECHNIQUE FÉDÉRALE DE LAUSANNE, 2014.
[64] C. Pichler, R. Lackner, and H. A. Mang, “A multiscale micromechanics model for the autogenous-shrinkage deformation of early-age cement-based materials,” *Eng. Fract. Mech.*, vol. 74, no. 1–2, pp. 34–58, Jan. 2007.